

Convective Heat Transport in Compressible Fluids

Akira Furukawa and Akira Onuki
 Department of Physics, Kyoto University, Kyoto 606-8502
 (December 27, 2021)

We present hydrodynamic equations of compressible fluids in gravity as a generalization of those in the Boussinesq approximation used for nearly incompressible fluids. They account for adiabatic processes taking place throughout the cell (the piston effect) and those taking place within plumes (the adiabatic temperature gradient effect). Performing two-dimensional numerical analysis, we reveal some unique features of plume generation and convection in transient and steady states of compressible fluids. As the critical point is approached, overall temperature changes induced by plume arrivals at the boundary walls are amplified, giving rise to overshoot behavior in transient states and significant noises of the temperature in steady states. The velocity field is suggested to assume a logarithmic profile within boundary layers. Random reversal of macroscopic shear flow is examined in a cell with unit aspect ratio. We also present a simple scaling theory for moderate Rayleigh numbers.

PACS numbers: 44.25.+f, 47.27.Te, 64.70.Fx

I. INTRODUCTION

Recently much attention has been paid to organized fluid motion in turbulent convection in the Rayleigh-Bénard geometry [1,7]. Although the conventional hydrodynamic equations are constructed for (nearly) incompressible fluids [8], we may mention a number of convection experiments in compressible one-component fluids in the supercritical region [9-19], together with those in non-critical fluids such as water or Hg [20-22]. In these studies the Nusselt number Nu representing the efficiency of convective heat transport has been measured at large values of the Rayleigh number Ra defined by

$$Ra = \frac{\rho g L^3 \beta (T_{\text{bot}} - T_{\text{top}})}{\eta} = D, \quad (1.1)$$

Here g is the gravity constant, $T = T_{\text{bot}} - T_{\text{top}}$ is the difference between the bottom and top temperatures, and L is the cell height. As the critical point is approached in one-component fluids, the thermal expansion coefficient $\beta = (\partial \rho / \partial T)_p$ grows strongly as $\beta \rightarrow \infty$ (in the same manner as the isothermal expansion coefficient $K_T = (\partial \rho / \partial p)_T$ and the isobaric specific heat C_p), the thermal diffusivity D decreases as $D \rightarrow 0$, and the shear viscosity η is nearly a constant. Here ξ is the thermal correlation length growing as $(T - T_c)^{-1}$ on the critical isochore with $\xi = 1.24$ and $\xi = 0.625$. Hence, in the critical region, Ra can be extremely large; for example, $Ra \sim 10^3$ even for not very long L (< 10 cm). The Prandtl number $Pr = \eta / \kappa = D$ was in the range of 1-100.

High compressibility of supercritical fluids gives rise to some unique features not encountered in incompressible fluids. (i) First, the transient behavior after application of a heat flux from the bottom is strongly influenced by the so-called piston effect [23-30], as revealed by recent high-precision experiments on ^3He [17] and reproduced by subsequent simulation [31]. (ii) Second, as β grows, the usual mechanism of convection

onset $Ra > Ra_c (= 1708)$ is replaced by that of the Schwarzschild criterion [32,33]. That is, for large compressible fluid columns (even far from the critical point), convection sets in when thermal plumes continue to rise upward adiabatically. This occurs when the applied temperature gradient $|dT/dz|$ is larger than the adiabatic gradient [34],

$$a_g = (\partial T / \partial p)_s g; \quad (1.2)$$

which is equal to 0.034 m K/cm for ^3He and 0.27 m K/cm for CO_2 . This is the condition that the entropy $s = s(T, p)$ per unit mass decreases with height as $ds/dz = (C_p/T) [dT/dz + a_g] < 0$, under which the entropy of fluid elements adiabatically convected upward is larger than that of the ambient fluid. More precisely, Gitterman and Steinberg [32] found that the convection onset for compressible fluids is given by $Ra^{\text{corr}} > Ra_c$, where Ra^{corr} is a corrected Rayleigh number defined by

$$Ra^{\text{corr}} = \left(\frac{\rho g L^3 \beta}{\eta} \right) (T - a_g L) = Ra (1 - a_g L / T); \quad (1.3)$$

This is a natural consequence because the effective temperature gradient seen by the rising plumes is given by $T/L - a_g$. At the convection onset we thus have

$$(T/L)_{\text{on}} = a_g L + Ra_c D = (g \beta L^3): \quad (1.4)$$

where the second term behaves as $(T - T_c)^{-1} L^3$ and can be much smaller than the first term even for small L ($\sim 1 \text{ mm}$ [16]) as $T \rightarrow T_c$. The relation (1.4) has been confirmed in SF_6 [11], and in ^3He [16]. (iii) Third, in steady convective states, experimental curves of $Ra(Nu - 1)$ vs Ra^{corr} were collapsed onto a single universal curve for various densities above T_c [12] and for various average reduced temperatures on the critical

isochore [16]. These empirical results are highly nontrivial, because Nu can in principle depend on Ra , Pr , and $a_g L = T_c$, while Nu is a function of Ra and Pr for incompressible fluids.

For various fluids under relatively large $T_c/a_g L$ (where $Ra^{corr} = Ra$), data of Nu have been fitted to a simple scaling law,

$$Nu \propto Ra^a : \quad (1.5)$$

The exponent a has been in a range from 0.28 to 0.31 and, in particular, a theoretical value $a=7/2$ [2,4] was generally consistent with data for $Ra < 10^{12}$ [9,18,21]. Moreover, measurements of the patterns of isothermals surfaces [20] and the velocity [21,22] have been informative on plume motion and a large-scale circulating shear flow in small-aspect-ratio cells [19,21]. Several authors have also performed numerical analysis of convection at large Ra in two dimensions (2D) [35,39] and in three dimensions (3D) [40,43]. Even in 2D salient features in the experiments have been reproduced. In these simulations, if the temperature is averaged over a long time, the temperature gradient is localized in thin boundary layers with thickness δ_T related to Nu by

$$Nu = L/\delta_T : \quad (1.6)$$

Both in 2D and in 3D (if visualized from side), the plumes tend to be connected from bottom to top for large Pr because of slow thermal diffusion, while they become diffuse far from the boundaries for small Pr . In the 3D simulations with periodic or free-slip sidewalls [42,43], local boundary shear flows were observed between incoming plumes and outgoing networks of buoyant sheets in horizontal planes close to the boundaries.

In this paper we will derive and examine hydrodynamic equations for compressible fluids under gravity in the supercritical region, in which the oscillatory motion of sound has been averaged out [23]. Since the time scale of convective motions is much longer than that of the acoustic wave $\tau_{ac} = L/c$ (typically of order 10^{-4} s for $L = 1$ cm), such a description is convenient theoretically and is even indispensable for numerical analysis. Our dynamic equations are a natural generalization of the usual hydrodynamic equations [8]. Our new predictions are unique particularly when the piston effect comes into play, as has been demonstrated in the previous simulation [31] relatively close to the convection onset. This paper will present 2D simulations of our hydrodynamic equations for much larger Ra^{corr} both in transient and (dynamic) steady states. Even in steady states, we will find some characteristic features of turbulent states, which have not been reported in the previous simulations [35,37,40,43], such as the logarithmic velocity profile of the velocity near the boundary [34] and random reversal of the large-scale circulating flow in small-aspect-ratio cells [19,21]. We will also point out that individual arrivals of plumes

at the boundaries cause global temperature fluctuations in the cell via the piston effect. The resultant noise level of the temperature fluctuations grows as the critical point is approached.

II. THEORETICAL BACKGROUND

A. Hydrodynamic equations

We consider a supercritical fluid on the critical isochore in a cell with the bottom plate at $z = 0$ and the top plate at $z = L$. The z axis is taken in the upward direction and the total fluid volume is fixed at V . The temperature disturbance $T(r;t) = T(r;t) - T_{top}$ measured from the temperature T_{top} at the top boundary is much smaller in magnitude than $T_{top} - T_c$. Hereafter \bar{T} will be used to denote the reduced temperature at the top boundary, which satisfies

$$\bar{T} = T_{top} = T_c - 1 \quad T = T_c : \quad (2.1)$$

We assume that the gravity-induced density stratification is not too severe such that the thermodynamic derivatives are nearly homogeneous in the cell. This is satisfied when $j = c - 1/j$ ($c = (\partial p/\partial T)_g L$) with $c = 0.33$ [44]. This condition is rewritten as

$$c + a_g L = T_c : \quad (2.2)$$

In the theoretical literature on convection [2,7], the top and bottom temperatures T_{bot} and T_{top} are constant parameters. However, in most of recent convection experiments, particularly in cryogenic ones, the heat flux at the bottom $Q = -(\kappa dT/dz)_{z=0}$ and T_{top} have been fixed. The κ is the thermal conductivity. Furthermore, if the top and bottom walls are made of a metal with high thermal conductivity, the boundary temperatures become homogeneous in the lateral directions (unless local temperature changes are too fast). Then $T_{bot}(t)$ and hence $\bar{T}(t)$ are functions of time only. Metcalfe and Behringer [45] performed linear stability analysis of convection onset under this cryogenic boundary condition. In the nonlinear regime it is of great interest how the boundary layer thickness and the plume generation depend on the boundary condition.

In equilibrium the pressure gradient is given by $g = c g$. In nonequilibrium we set

$$p(r;t) = p_0 - c g z + p_1(t) + p_{inh}(r;t); \quad (2.3)$$

where p_0 is a constant, $p_1(t)$ and p_{inh} are the homogeneous and inhomogeneous parts induced by \bar{T} , respectively. That is, we assume $\langle p_{inh} \rangle = 0$, where $\langle \cdot \rangle = \frac{1}{V} \int d\mathbf{r} (\cdot)$ represents the space average. The p_{inh} is related to the space average of \bar{T} by

$$p_1(t) = (\partial p / \partial T)_h T_i(t); \quad (2.4)$$

which follows from the thermodynamic relation $dp = (\partial p / \partial T)_T dT + (\partial p / \partial T)_T dT$ and the condition that the space average of the density deviation vanishes ($\bar{\rho}_i = 0$). It is important that the combination $p(r;t) + \rho_0 g z$ is nearly homogeneous or $p_1(t) \approx p_{inh}(r;t)$ for uid motions much slower than the acoustic time $t_{ac} = L/c$ ($c \approx 10^4$ cm/s being the sound velocity) [24,46]

Now we derive the equation for T from the heat conduction equation

$$T \frac{\partial}{\partial t} + v_r s = -\kappa \nabla^2 T; \quad (2.5)$$

where $s(r;t)$ is the entropy per unit mass. Here s consists of the equilibrium part $s_{eq}(z)$ with

$$\frac{d}{dz} s_{eq}(z) = \frac{\partial s}{\partial p}_T g = T^{-1} C_p a_g \quad (2.6)$$

and the nonequilibrium deviation,

$$s(r;t) = T^{-1} C_p T(r;t) - \frac{\partial T}{\partial p}_s p_1(t); \quad (2.7)$$

With the aid of the thermodynamic identity $(\partial T / \partial p)_s = (\partial T / \partial p)_T (1 - \beta_s)$, we rewrite (2.5) to obtain the desired equation for T ,

$$\frac{\partial}{\partial t} + v_r D^2 T = \kappa \nabla^2 T + s \frac{d}{dt} T_i; \quad (2.8)$$

where $D = -C_p$ is the thermal diffusivity and

$$\beta_s = 1 - \beta_s; \quad (2.9)$$

The specific heat ratio β_s behaves as

$$\beta_s = C_p / C_v \rightarrow 1; \quad (2.10)$$

where C_p and C_v are the specific heats (per unit volume) at constant p and V , respectively, with $\beta_s \rightarrow 0.1$. The first term on the right hand side of (2.8) arises from $ds_{eq} = dz$. Inside plumes the temperature is adiabatically cooled if they go upward ($v_z > 0$), or adiabatically warmed if they go downward ($v_z < 0$). In this way this term suppresses upward motion of warmer plumes from the bottom and downward motion of cooler plumes from the top, resulting in the Schwarzschild criterion of convection onset (the adiabatic temperature gradient effect). On the other hand, the second term arises from $p_1(t)$, leading to the piston effect [24]. It is worth noting that the space integral of (2.8) in the cell becomes

$$V C_v \frac{d}{dt} T_i = \oint da n_r T; \quad (2.11)$$

where use has been made of $\bar{h} v_i = 0$. The right hand side represents the rate of heat supply from the boundary surface, where da is surface element and n is the

outward surface normal. Its time-integration is the total heat supply expressed as $V \bar{h} s_i$, resulting in

$$C_v \bar{h} T_i(t) = \bar{h} s_i(t); \quad (2.12)$$

which also follows (2.4) and the space average of (2.7). The appearance of C_v in on the left hand side of (2.12) is a natural consequence under the fixed volume condition. Notice that (2.7) can also be written as

$$T(r;t) = \frac{T}{C_p} s(r;t) + T \frac{1}{C_v} - \frac{1}{C_p} \bar{h} s_i(t); \quad (2.13)$$

This relation holds even in gravity if s is the deviation of $s_{eq}(z)$ as in (2.7). In addition, the density deviation ρ_i is written in our approximation as

$$\rho_i = K_T g(z - L/2) - \rho_p (T - \bar{h} T_i); \quad (2.14)$$

where $K_T = (\partial \rho / \partial p)_T$ and we have set $\bar{h} i = 0$.

Since $C_p \approx C_v$ near the critical point, the homogeneous part of T (second term) in (2.13) can easily dominate over the inhomogeneous part (first term) even when s is localized near a heated wall. Indeed, if a thermal disturbance is produced within a thermal boundary layer with thickness δ near the boundary, the ratio of the homogeneous part ($\bar{h} s_i$) to the localized inhomogeneous part (ρ_i) in (2.13) is of order $(\beta_s - 1)^{-1/2} L$ where L is the characteristic system length. Temperature homogenization is achieved when $(\beta_s - 1)^{-1/2} L$. By setting $\delta = (\rho \tau_1)^{1/2}$ we obtain the time constant of this thermal equilibration (the piston time) in the form,

$$\tau_1 = L^2 D (\beta_s - 1)^2; \quad (2.15)$$

Next we consider the momentum equation for the velocity field $v(r;t)$. On long time scales, sound waves decay to zero and the incompressibility condition

$$\nabla \cdot v = 0 \quad (2.16)$$

becomes nearly satisfied ($\tau_{hom} \rightarrow 0$) [46]. Then the dissipation of v is produced by the shear viscosity and the usual Navier-Stokes equation in the Boussinesq approximation may be set up in the form [1],

$$\frac{\partial}{\partial t} + v_r v = \kappa \nabla^2 v + \rho_p g T e_z + -r^2 v; \quad (2.17)$$

where the inhomogeneous part p_{inh} ensures (2.16), e_z is the unit vector along the z axis, and ρ is the average density. The two equations (2.8) and (2.17) are our fundamental dynamic equations closed under (2.16). In the conventional theory [1,8], (2.17) has been used, but the right hand side of (2.8) vanishes.

As another characteristic feature near the critical point, the Prandtl number behaves as

$$Pr = D : \quad (2.18)$$

For example, $Pr = 350$ at $T = T_c - 1 = 10^3$ in ^3He . This means that the time scale of the thermal diffusion is much slower than that of the velocity in the critical region. Based on this fact, the simulation in Ref. [31] was performed using the Stokes approximation in which the left hand side of (2.17) is set equal to zero. Good agreement with the experiments [17] was then obtained for $Ra^{corr} = Ra_c - 1 < 5$ at $\epsilon = 0.05$.

For $Pr \gg 1$, let us estimate the upper bound of Ra^{corr} below which the Reynolds number Re is smaller than 1 or the Stokes approximation is allowable. The characteristic temperature variation $(T)_h$ changing perpendicularly to the z axis and the characteristic velocity field v_{p1} are related by

$$v_{p1} = (\rho_c g = k^2) (T)_h; \quad (2.19)$$

where $k = 2\pi/L$ for roll patterns. If $Ra^{corr} = Ra_c$ is considerably (but not much) larger than 1, $(T)_h = T$ is of order 1 (but somewhat smaller than 1). Then we obtain

$$v_{p1} = (Ra^{corr} = Ra_c) D = L; \quad (2.20)$$

Thus the small Reynolds number regime is written as

$$Ra^{corr} = Ra_c < Pr; \quad (2.21)$$

where use has been made of $Re = v_{p1} L = 1$. For $Pr \gg 1$ there is a sizable range of Ra^{corr} in which the Stokes approximation is justified. In passing, for $0 < Ra^{corr} = Ra_c - 1 \ll 1$, the theory of the amplitude equation [48] predicts

$$v_{p1} L = D \quad (T)_h = T \quad (Ra^{corr} = Ra_c - 1)^{1/2}; \quad (2.22)$$

from which we have $Nu \gg 1$ for $Ra^{corr} = Ra_c - 1$ because the convective heat current is of order $C_p (T)_h v_{p1}$. In the next section we will estimate v_{p1} for much larger Ra .

Analogously to (2.19), the inhomogeneous pressure deviation p_{inh} is estimated as $p_{inh} = (\rho_c g = k^2) (T)_h$. If we assume $p_1(t) = (\partial p / \partial T)_s T$ from (2.4) and $(T)_h$ as in (2.20), we find that $p_{inh} = p_1(t)$ is of order $a_g = T_c k$ and is much smaller than 1 from (2.2). This estimation justifies the assumption of the homogeneity of $p(r; t) + \rho_c g z$ made below (2.4).

B. Free energy and heat production rate

In the presence of small deviations of the temperature and the density, T and ρ , around an reference equilibrium state, we have an increase of the free energy functional F . Up to the bilinear order of the deviations, it is of the form [23,47],

$$F = \int^Z dr \frac{C_V}{2T} (T)^2 + \frac{1}{2^2 K_T} (\rho)^2 + g z; \quad (2.23)$$

where the third term is the potential energy in gravity. All the deviations are assumed to change slowly in space compared with the thermal correlation length ξ . If we express ρ in terms of T as in (2.14), we obtain

$$F = \frac{1}{2T} \int^Z dr C_p (T - T_h)^2 + C_V \int^Z dr T^2; \quad (2.24)$$

where the constant term is omitted. We notice that F decreases dramatically for $\epsilon \ll 1$ in the process of adiabatic temperature homogenization. Furthermore, in the presence of velocity field, the total free energy change is the sum of F and the kinetic energy of the velocity field,

$$F_K = \frac{1}{2} \int^Z dr v^2; \quad (2.25)$$

Its time derivative is calculated from our dynamic equations (2.7) and (2.17) in the form,

$$\frac{d}{dt} (F + F_K) = \int^R dr \left(\frac{\partial}{\partial t} (T_{th} + T_{vis}) + \frac{1}{T} \nabla \cdot [T(n - r T)] \right); \quad (2.26)$$

where T_{th} and T_{vis} are the thermal and viscous heat production rates (per unit volume) [34], respectively, defined by

$$T_{th} = T^{-1} \nabla \cdot T^2; \quad (2.27)$$

$$T_{vis} = \sum_{ij} X_{ij} (\partial v_i / \partial x_j)^2; \quad (2.28)$$

In the second term of (2.26) the surface integral is over the boundary of the cell, n being the outward unit vector. In terms of the heat flux from the bottom Q , it is expressed as $\nabla \cdot Q = T L$ if the top temperature is fixed.

C. Basic relations in steady states

We consider steady convective states in the Rayleigh-Bénard geometry, in which the flow pattern is either time-independent not far above the convection onset or chaotic at larger Ra . We treat T as a constant parameter. Under the condition of fixed heat flux at the bottom, however, $T(t)$ exhibits rapidly-varying fluctuations in chaotic states. In this case T in the following relations represents the time-average of $T(t)$. The steady state averages (over space and time) will be denoted by \bar{h}_s in order to distinguish them from the space averages \bar{h} used so far.

We make (2.8) and (2.17) dimensionless by measuring space and time in units of L and $L^2 = D$ and setting $\mathbf{r} = L^{-1} \mathbf{r}$ and $\tau = D L^{-2} t$. The temperature deviation is written as

$$T(r; \tau) = T = 1 + z + Ra^{-1} F(r; \tau); \quad (2.29)$$

where $z = z/L$. The dimensionless function F becomes nonvanishing in convective states and obeys

$$\frac{\partial}{\partial \tau} + V \frac{\partial}{\partial z} - \frac{\partial^2}{\partial z^2} F = Ra^{corr} V_z + \frac{d}{dt} h F i; \quad (2.30)$$

where $\tilde{r} = Lr$ is the space derivative in units of L . Then the (average) heat flux at the bottom is written as $Q = (T=L)[1 + Ra^{-1} f]$, where

$$f = -h(\langle F \rangle_{z=0} i_s); \quad (2.31)$$

The f is a function of Ra^{corr} and Pr . The Nusselt number $Nu = QL = T$ is expressed as

$$Nu = 1 + Ra^{-1} f; \quad (2.32)$$

As the boundary condition of F we require $F = 0$ at $z = 0$ and 1 if T_{top} and T_{bot} are fixed. However, if T_{top} and Q at the bottom are fixed, we have $F = 0$ at $z = 0$ and $\langle F \rangle = \langle z \rangle = Ra(Nu - 1)$ at $z = 0$. The dimensionless velocity $V(\tilde{r}; \tau) = (L=D)v$ obeys

$$\frac{1}{Pr} \frac{\partial}{\partial \tau} + V \frac{\partial}{\partial z} V = \tilde{r} P_{inh} + F e_z + \tilde{r}^2 V; \quad (2.33)$$

where P_{inh} ensures $\tilde{r} V = 0$.

Here we assume that the piston term, the second term on the right hand side of (2.30), can be neglected in steady states. For $\epsilon = 0.05$, the piston term in steady states is less than a few percents of the convection term $v \tilde{r} F$ in (2.30) except at the boundaries. It thus produces no significant effects on steady state heat transport (on Nu), while it can be crucial in the initial transient stage [31]. Then, if the piston term in (2.30) is neglected, (2.30) and (2.33) become of the same form as those of usual incompressible fluids except that Ra^{corr} appears in place of Ra . A much smaller ϵ , however, this assumption is questionable, because the noise part of $h F i$ grows as $1/\epsilon$, as will be discussed later in the next section. We may conclude the following (at least for $\epsilon = 0.05$). (i) It follows the Gitterman-Steinberg criterion $Ra^{corr} > Ra_c$ in convective states in the compressible case [32,33]. (ii) It is more nontrivial that the combination

$$Ra(Nu - 1) = f(Ra^{corr}; Pr) \quad (2.34)$$

should be a universal function of Ra^{corr} and Pr from (2.32) in agreement with the experiments [12,16]. Notice that $Ra(Nu - 1) = f(Ra; Pr)$ holds for incompressible fluids in terms of the same f . These experiments and more decisively that by Ahlers and Xu [15] indicate that f should be nearly independent of Pr once Pr considerably exceeds 1. In the 3D simulation by Verzioco and Camussi [41], Nu became independent of Pr for $Pr > 0.5$. Theoretical support of this behavior using scaling arguments was presented in Ref. [7].

In steady states we may also derive some exact relations for variances among T and v . Using the dynamic equations (2.8) and (2.17) we calculate the averages of $\langle (T)^2 \rangle = \langle T^2 \rangle$, $\langle v^2 \rangle = \langle v^2 \rangle$, and $\langle (z - T) \rangle = \langle z - T \rangle$ to obtain

$$h \langle T^2 \rangle i_s = a_{th}^2 + a_{th}(a_{th} - a_g)(Nu - 1); \quad (2.35)$$

$$\langle h(v_i - \langle v_i \rangle)^2 i_s \rangle = Ra(D=L)^2 (Nu - 1); \quad (2.36)$$

We also obtain a cross correlation,

$$h v_z T i_s = a_{th} D (Nu - 1); \quad (2.37)$$

which is nothing but the average convective heat flux (if C_p is multiplied). Here $a_{th} = T=L = -hdT/dz$ is the average temperature gradient and a_g is the adiabatic temperature gradient defined by (1.2). If we use the usual hydrodynamic equations for incompressible fluids, the right hand side of (2.35) becomes $a_{th}^2 Nu$, while (2.36) and (2.37) remain the same [2]. In addition, (2.35) indicates $a_{th} > a_g$ in convective states in which $Nu > 1$. This is consistent with the convection criterion $Ra^{corr} > Ra_c$. We obtain the averages of the two dissipation rates in (2.27) and (2.28) by multiplying ϵT and ϵ to (2.35) and (2.36), respectively. Using the thermodynamic identity $T_p = C_p (\langle T \rangle = \langle p \rangle)_s$, we obtain

$$h_{th} i_s + h_{vis} i_s = T^{-1} a_{th}^2 Nu; \quad (2.38)$$

$$(h_{th} i_s - T^{-1} a_{th}^2) = h_{vis} i_s = a_{th} = a_g - 1; \quad (2.39)$$

The first relation (2.38) also follows from the average of (2.26). The second relation (2.39) holds only in convective states ($Nu > 1$), while the right hand side is replaced by $C_p a_{th} = T_p / \rho g = a_{th} = a_g$ for the usual hydrodynamic equations of incompressible fluids.

III. SIMULATION RESULTS

We perform numerical analysis of (2.8) and (2.17) in 2D using parameters of ^3He in a cell with $L = 1.06 \text{ mm}$. The reduced temperature is $\epsilon = 0.05$ (except in Fig.13), where $\epsilon_s = 22.8$; $T_p = 26.9$, $\epsilon = 1.88 \times 10^4 \text{ erg}/(\text{cm}^2 \text{ s K})$, $D = 5.42 \times 10^5 \text{ cm}^2/\text{s}$, and $Pr = 7.4$ [16,17,31]. The condition (2.2) is well satisfied. The piston time t_1 in (2.15) is given by 0.42 s . We apply a constant heat flux Q at the bottom $z = 0$ for $t > 0$ with a fixed top temperature T_{top} at $z = L$. In steady states we have $Ra^{corr} = Ra_c = 0.90 [T = a_g L - 1]$; where $a_g L = 3.57 \text{ K}$. Thus $(T)_{on} = 7.6 \text{ K}$ and $Q_{on} = 13.5 \text{ nW}$ at the convection onset. We assume homogeneity of the boundary temperatures, T_{top} and T_{bot} , in the lateral x direction.

In the experiments the aspect ratio was 57, so in the simulation [31] the periodic boundary condition was imposed in the x direction with period $4L$. This period

was chosen because the roll period is close to $2L$ slightly above the onset for infinite lateral dimension [1]. Then, in steady states in the region $1 < Q = Q_{\text{on}} < 5$, the linear relation

$$Q = Q_{\text{on}} + 1 = A_0 [T = (T)_{\text{on}} + 1] \quad (3.1)$$

was numerically obtained with $A_0 = 2.2$ in good agreement with the experiments. From $Nu = Q = T = Q_{\text{on}} = (T)_{\text{on}}$, the behavior of Nu is known from (3.2) in the range $1 < Q = Q_{\text{on}} < 5$. In particular, slightly above the onset, we have

$$Nu + 1 = A_1 (Ra^{\text{corr}} = Ra_c + 1) + \quad : \quad (3.2)$$

where $A_1 = 0.64$ in fair agreement with the theoretical value ($A_1 = 0.70$ for $Pr = 7.4$) [49]. This behavior is also consistent with (2.22).

In this work we are interested in fluid motion for relatively large Ra up to $3 \cdot 10^6$. In the following we show two sets of the numerical results. In the first set, periodic sidewalls are assumed at $x = 0$ and $x = L_z$ with period $L_z = 4L$ as in Ref. [31]. In Table 1 the steady state values of T , Ra^{corr} , Ra , Nu , and Re are written, where Re is a Reynolds number to be defined in (3.11). They are obtained for $Q = 0.0458 \text{ W/cm}^2 (= 3.4Q_{\text{on}})$, $0.965 \text{ W/cm}^2 (= 71Q_{\text{on}})$, and $122.2 \text{ W/cm}^2 (= 9 \cdot 10^3 Q_{\text{on}})$. For the smallest Q the system tends to a time-independent convective state, as already studied in Ref. [31], while for the other values of Q the system tends to a chaotic state without macroscopic boundary shear flow. In the second set, we perform simulations for $A = 1/2$; and 3 with insulating and rigid sidewalls at $x = 0$ and AL , at which $v = 0$ and through which there is no heat flux ($\partial T = \partial x = 0$), as will be presented in Figs. 4, 12, and 13.

In addition, if the temperature difference will be simply written as T , it should be taken as the time average of $T(t)$ in a steady state. We also assume that Pr is considerably larger than 1 in the following arguments.

A. Transient behavior

In Fig. 1 we show numerically calculated $T(t) = T_{\text{bot}}(t) - T_{\text{top}}$ for $Q = 0.965 \text{ W/cm}^2$ in (a) and for $Q = 122.2 \text{ W/cm}^2$ in (b). They nearly coincide with the upper broken curve without convection ($v = 0$) in the initial stage before the maximum is attained. The latter curve is calculated from (2.8) as

$$[T(t)]_0 = \frac{Q}{\frac{r}{D} t} \int_0^Z \frac{1}{P} \frac{ds}{s} \frac{1}{s + t = t_1} e^s; \quad (3.3)$$

where t_1 is defined by (2.15) and the integral in the brackets behaves as $(t = t_1)^{1/2}$ for $t \rightarrow t_1$ [23]. If the piston

term is absent and $v = 0$, (2.8) becomes the simple diffusion equation, yielding $[T(t)]_0 = (2Q =) (Dt =)^{1/2}$, which is about half of $[T(t)]_0$ in (3.3) for $t \rightarrow t_1$ (see Fig. 3 in Ref. [31]). We also show the numerically calculated $T(t)$ at fixed pressure where the piston term is absent ($\sigma_s = 0$ in (2.8)) but $v \neq 0$. In (a) the experimental curve is shown to have a lower peak and overdamp more slowly than in our simulation. In (b) the selected value of Q is in the region where no overshoot was observed in the experiment. See also Fig. 11, where the numerical curves of $T(t)$ will be given for other choices of the parameters.

In Fig. 2 we show time evolution of the temperature profile at $Q = 122.2 \text{ W/cm}^2$ for periodic sidewalls. In (A) and (B) small-scale mushroom-like plumes are ejected from the bottom. In (C) and (D) they reach the top and are attenuated there. In this initial stage the typical raising speed v_{p1} is estimated as $L = t_{\text{tr}}$ where t_{tr} is the traversing time. From (A)–(C) we find that it is nearly equal to the free-fall velocity v_g defined by

$$v_g = (Lg_p T)^{1/2} = (RaPr)^{1/2} D = L; \quad (3.4)$$

which is 2.37 cm/s . In this case the plumes leave the bottom at zero velocity and go upward with their velocity roughly of the form,

$$v_{p1}(t) = v_1 + 1 \exp[-(t - t_0)/t_{\text{vis}}]; \quad (3.5)$$

where t_0 is the departure time, $t_{\text{vis}} = R^2 =$ is the viscous relaxation time with R being the plume size, and

$$v_1 = R^2 g_p T = \quad (3.6)$$

is the terminal velocity achieved by balance between the buoyancy and the viscous drag. For $t_{\text{tr}} \rightarrow t_{\text{vis}}$ the viscous drag is negligible and we have $v_{p1}(t) \rightarrow v_g^2(t - t_0) = L$ and $t_{\text{tr}} = L = v_g$. Thus, if the initial velocity is much less than v_g , the free-fall condition becomes

$$R = L = (Pr = Ra)^{1/4}; \quad (3.7)$$

under which $v_1 = (R = L)^2 (Ra = Pr)^{1/2} v_g = v_g$. In Fig. 2, $R = L = 1/3$ and $(Pr = Ra)^{1/4} = 0.04$, so the above condition is satisfied.

With the arrival of the plumes the heat current increases at the top, because T_{top} is fixed, and a negative deviation of σ is produced in a layer near the top. As can be known from (2.13), the piston effect is then operative, resulting in a homogeneous lowering of the temperature in the whole cell. In the time region around (E) the fluid is vigorously mixed with high Reynolds numbers. More precisely, the height-dependent Reynolds number $\hat{Re}(z; t)$ to be defined in (3.12) below is about 20 except in the vicinity of the boundaries. A downward flow of cooler fluid regions is then produced from the top. In the steady state (F), the temperature deviation becomes considerably smaller than in the transient states,

and the localized boundary shear flows are produced between outgoing and incoming plumes with thickness ℓ_v much smaller than L .

The overshoot is more clearly illustrated in Fig.3, which displays the average of $T(x; z; t)$ taken in the x direction,

$$\overline{T}(z; t) = \frac{1}{L} \int_0^L T(x; z; t) dx; \quad (3.8)$$

for the points (A), (C), (E), and (F) in Fig.1b. As a characteristic feature, the temperature in the interior consists of global changes due to the piston effect and bumps due to localized plumes. In (E) the cooler layer becomes thicker temporarily near the top due to the excess heat flow.

In our simulation the raising plumes leave the bottom and reach the top nearly simultaneously, resulting in a homogeneous temperature change. (i) Not far above the onset this mechanism is the main cause of the overshoot in compressible fluids. Note that a small peak appears in $T(t)$ even in the fixed pressure case ($\beta_s = 1$) as shown in Fig.2 of Ref. [31] and as was observed by Behringer and Ahlers [50]. Furthermore, in Ref. [31], the time scale of the overshoot (from the maximum to the minimum of $T(t)$) due to the piston effect was predicted to be of order $t_D = (Ra^{corr} = Ra_c - 1)$, where $t_D = L^2/4D$ (≈ 50 s) is the diffusion time. This fairly agrees with later analysis of the experimental data [51]. (ii) For much larger Q such as those in Figs.1a and 1b, however, the downward flow from the top is also rapid enough to produce large overshoot, as demonstrated by the curves at fixed (height-dependent) pressure. Whether fixed is the volume or the pressure, the time scale of the overshoot is of the order of the traversing time L/v_g of the plumes due to gravity.

As regards the overshoot behavior of $T(t)$, agreement between our simulation and the experiment [17] becomes worse with increasing Q . We point out the possibility that in the experiment a synchronous arrival of plumes at the top might have not been realized for very large Q or for very short L/v_g because of large lateral dimensions of the cell used. That is, if some plumes arrive at the top and others leave the bottom at the same time, negative interference between currents up and down will suppress overshoot.

B. Steady state behavior

Now we discuss the Nusselt number Nu in steady states. Fig.4 shows the combination $Ra^{corr}(Nu - 1) = (Ra^{corr} - Ra_c)$ vs $Ra^{corr} = Ra_c - 1$ for periodic sidewalls and for $A = 1; 2$; and 3 . This combination depends on Ra^{corr} and A from (2.34) in steady states. The data (solid line) [17] excellently agree with the numerical

results for periodic sidewalls. We find that the scaling relation (1.5) nicely holds for $Ra^{corr} = Ra_c > 10$ for periodic sidewalls, while it holds only for $Ra^{corr} = Ra_c > 10^3$ at $A = 1$. The exponent a in (1.5) is close to $2/7$, but $a = 1/4$ is also consistent with our numerical data. If $A \rightarrow 1$ and Ra^{corr} is not very large such that the plume size is of order L , large-scale fluid motions are suppressed by the rigid sidewalls. This marked tendency of the A -dependent crossover of Nu was already reported in measurements for $A = 0.5; 1$, and 6.7 [10]. It was also confirmed in the 3D simulation by Kerr [42] for periodic sidewalls.

In Fig.5 we show the steady-state temperature deviation $\overline{T}(z)$ averaged in the x direction as in (3.8) and in time for the three values of Q in Table 1 for periodic sidewalls with period $L_z = 4L$. The averages taken along the x direction become only weakly fluctuating in time in steady chaotic states (the relative fluctuations being of order 10% for the largest Q). As has been observed ubiquitously in the previous simulations, the temperature gradient becomes localized within thermal boundary layers with thickness ℓ_T . Because $T = 2\ell_T Q = \ell_T L$, it is related to Nu by (1.6). The arrows in Fig.5 represent the maximum points, $z = \ell_v$ and $L - \ell_v$, of the variance of the horizontal velocity defined by

$$v_x(z) = \frac{1}{L} \int_0^L \frac{dx}{L} v_x(x; z; t)^2 \quad (3.9)$$

In Fig.6 we plot the normalized velocity variances, $v_x(z)/v_g$ in (a) and $v_z(z)/v_g$ in (b), where v_g is defined by (3.4) and

$$v_z(z) = \frac{1}{L} \int_0^L \frac{dx}{L} v_z(x; z; t)^2 \quad (3.10)$$

The time average of v_x^2 and v_z^2 in the brackets is also taken in these figures. On one hand, v_x take maxima at $z = \ell_v$ and $L - \ell_v$, where ℓ_v is hardly distinguishable from ℓ_T . On the other hand, v_z is largest at the middle of the cell. We also find that the sum (the kinetic-energy variance) $(v_x)^2 + (v_z)^2$ is nearly constant in the interior, which was a finding reported in Ref. [42]. At large Ra the maxima of v_x and v_z are of the same order and will be identified as the typical plume velocity v_{p1} . In our simulation we have $v_{p1} \approx 0.1 v_g$ ($/ Ra^{1/2}$), which is consistent with velocity measurements [9,22].

Kerr and Herring [43] made similar plots of the height-dependent velocity variances in their 3D simulations for free-slip sidewalls. They found that the characteristic length ℓ_v defined by the peak positions of $v_x(z)$ becomes longer than $\ell_T = L/2Nu$ with increasing Ra ; for example, for $Pr = 7$ they obtained $\ell_v = \ell_T - 1$ at $Ra = 10^4$ and $\ell_v = \ell_T - 3$ at $Ra = 10^7$. Verzicco and Camussi obtained a similar slow growing of $\ell_v = \ell_T$ at large Ra for $Pr > 1$ in their 3D simulation with $A = 1$ [41]. Also similarly, our 2D simulation with $Pr = 7.4$ gives $\ell_v = \ell_T = 2.54$ and

1.1 for $Q = 122.2$ and 0.965 $W = \text{cm}$, respectively, but we cannot draw a definite conclusion because of our limited range of Ra .

In Fig.7 we plot an overall Reynolds number \bar{Re} vs $R^{corr} = R_c - 1$ in the simulation for periodic sidewalls. It is defined by

$$\bar{Re} = - \frac{1}{h} \frac{\int_0^L \langle \tau \rangle dz}{\int_0^L \langle v_x^2 \rangle dz} \quad (3.11)$$

where the averages are taken in the whole space region. The \bar{Re} is smaller than 1 for $R^{corr} = R_c < 5$ [31]. For larger values of R^{corr} , it exceeds 1 and the effective exponent $\partial(\ln \bar{Re})/\partial(\ln Ra^{corr})$ is from 1=4 to 1=3. However, as suggested by Fig.6, the strength of the velocity fluctuations strongly depends on the distance from the boundary, so it is more informative to introduce a height-dependent Reynolds number,

$$\hat{Re}(z) = - \frac{1}{h} \frac{\int_0^L \langle \tau \rangle dz}{\int_0^L \langle v_x^2 \rangle dz} \quad (3.12)$$

where the time averages of the integrands are taken. As shown in Fig.8, $\hat{Re}(z)$ takes maximum at $z = \delta_v$ and $L - \delta_v$ of order

$$\hat{Re}(\delta_v) = \delta_v v_{p1} = ; \quad (3.13)$$

where $v_{p1} = v_x(\delta_v)$. This relation indicates $\hat{Re}(\delta_v) = Ra^{1/2}$ with $a = 2=7$ from $v_{p1} = 0.1v_g$ and $\delta_v = \frac{1}{2}$. The $\hat{Re}(z)$ becomes considerably smaller in the interior than at $z = \delta_v$, whose origin is the sparseness of the plumes in the interior (see (3.20) below). We confirm that Re is of the order of the space average $\frac{1}{L} \int_0^L \hat{Re}(z) dz = L$. In the literature [27], however, the (large-scale) Reynolds number has been identified as $Re = v_{p1}L =$, which is much larger than $\hat{Re}(\delta_v)$ in (3.13) by $L = \delta_v$. (For roll patterns, as was discussed below (2.21), we uniquely have $Re = v_{p1}L =$.)

At very large Ra the boundary layers should gradually crossover from a laminar state to a turbulent state except within thin viscous sublayers with thickness z_0 much shorter than δ_v . In the inertial region $z_0 < z < \delta_v$ of the boundary layer, it is natural to expect the logarithmic velocity profile [34],

$$v_x(z) = b_0 \tau_0^{1/2} [\ln(z/z_0) + c_0]; \quad (3.14)$$

where τ_0 is the amplitude of the shear stress at the boundary with b_0 and c_0 being dimensionless numbers of order 1. We may set $\tau_0 = \lim_{z \rightarrow 0} D_{xz}(z)$, where $D_{xz}(z)$ is the variance of the velocity gradient,

$$D_{xz}(z) = \frac{1}{L} \int_0^L \frac{dx}{L} \left(\frac{\partial}{\partial z} v_x(x; z; t) \right)^2 \quad (3.15)$$

Then $v_x(z) = (\tau_0)^{1/2} z$ as $z \rightarrow 0$. It is appropriate to define z_0 by [34]

$$z_0 = (\tau_0)^{1/2}; \quad (3.16)$$

which ensures $\hat{Re}(z_0) = 1$. The size of τ_0 should be equal to the typical size of $v_x v_z$ at $z = \delta_v$ even if we consider localized shear flows, so we also have

$$\tau_0 = \frac{1}{2} v_{p1}^2; \quad (3.17)$$

The ratio of the two lengths z_0 and δ_v is given by

$$\delta_v/z_0 = \frac{1}{2} \hat{Re}(\delta_v); \quad (3.18)$$

which grow with increasing Ra . In Fig.9a, $v_x(z)$ is fitted to the above logarithmic form in the inertial region for $Q = 122.2$ $W = \text{cm}$, where $(\tau_0)^{1/2} = 0.067v_g = 0.16 \text{ cm/s}$, $b_0 = 1.2$; $c_0 = 0.97$; and $z_0 = 0.025L$. In Fig.9b, we plot $v_x(z)$ and $zD_{xz}(z)$ on a logarithmic scale. We may conclude that these quantities do not behave as z in the inertial region of the boundary layers, although our Ra is not large enough to unambiguously demonstrate the logarithmic velocity profile. Here we point out that our results are not consistent with Shiraian and Siggia's primary assumptions of $\delta_v < \delta_v$ and the linear profile of the mean shear flow, v_x/z , in the region $z < \delta_v$ [2,3].

In contrast to the averages taken along the x direction, those taken along the z direction are rapidly varying functions of time at large Ra due to the random plume motions. We consider the vertical velocity variance defined by

$$v_z(x; t) = \frac{1}{L} \int_0^L \frac{dz}{L} v_z(x; z; t)^2 \quad (3.19)$$

In Fig.10 we display snapshots of $v_z(x; t)$, where the time average is not taken and peaks arising from the plumes become more apparent with increasing Q . For our Ra realized, the space regions occupied by the plumes become more sparse with increasing Ra in the interior. As the plumes move through the cell, they remain distinguishable from the ambient fluid because the thermal diffusion length $(D L = v_{p1})^{1/2}$ does not much exceeds δ_v . So we may define the volume fraction of the plumes ϕ_{p1} . The convective heat current is of order $\phi_{p1} v_{p1} C_p T \Delta T = L$, leading to

$$\phi_{p1} = \frac{1}{D} v_{p1}; \quad (3.20)$$

which is of order $Pr^{-1} \hat{Re}(\delta_v)^{-1} = 1$ from (3.13). For much larger Ra , the plumes will generate smaller scale eddies, ultimately leading to fully developed turbulence in the interior, as will be discussed in Section 4.

C. Overall Temperature Fluctuations

When a plume with a volume V reaches the boundary, it transfers a heat of order $C_p T V$ to the boundary wall. As indicated by (2.13), the piston effect then gives rise to a homogeneous change in $h T_i(t)$ of order

$$(\Delta T)_{\text{eff}} \approx (V/V_0) \Delta T: \quad (3.21)$$

Of course, the real plumes are extended objects and are continuously arriving at the boundary in high Ra convection. Thus $V_{p1} = V$ in the above formula should be regarded as the fluctuation amplitude of the plume volume fraction ϕ_{p1} in the interior, although we do not know its dependence on Ra etc at present. If T_{top} and Q at the bottom are fixed as in our simulation, $T(t)$ should also consist of fluctuations of the same origin. Because of the strong critical divergence of ϕ_{p1} , we expect that the relative amplitude $(\Delta T)/T = \Delta T/T$ would increase as ϕ_{p1} is decreased with a fixed size of T .

Fig.11 displays time sequences of $h T_i(t)$ and $T(t)$ at fixed volume and pressure for periodic sidewalls with $L_z = 4L$, which demonstrates strong correlations between these two deviations at fixed volume. In case (a) (upper figure) we set $\phi_{p1} = 0.05$ ($s = 22.8$), $T = 0.17 \text{ mK}$, $Pr = 7.4$, $Ra = 7.38 \times 10^4$, and $Nu = 4.06$, while in case (b) (lower figure) we set $\phi_{p1} = 0.01$ ($s = 119$), $T = 0.19 \text{ mK}$, $Pr = 37.7$, $Ra = 4.14 \times 10^5$, and $Nu = 6.04$. The steady state values of T in the two cases are chosen to be only slightly different. At fixed volume, the fluctuations of $h T_i(t)$ and $T(t)$ are strongly correlated, and are larger and slower for (b) than for (a) in steady states ($t > 100$). This is because of the critical enhancement of the piston effect and the critical decrease of D with decreasing ϕ_{p1} . At fixed pressure, where the piston effect is absent, $T(t)$ exhibits noises much smaller than those at fixed volume and $h T_i(t)$ smoothly changes in time. It is worth noting that this noise increase at fixed volume accompanied with an increase of Ra is contrary to the usually measured noise behavior of the temperature. For non-critical fluids, if the temperature is measured at the center of a cell, its fluctuation amplitude divided by T is known to decrease with increasing Ra as Ra^{-n} . The exponent n was about 0.15 in a cell with $A = 1$ [4,18].

D. Random Reversal of Macroscopic Flow

For a convection cell with $A = 1$, it is well known that large-scale shear flow develops near the boundary of the cell for large enough Ra [19,21,22]. Moreover, it has also been observed that the global circulation changes its orientation over long time scales [21,19]. For the case of $A = 1$, $\phi_{p1} = 0.05$, $Q = 40.7 \text{ W cm}^{-2}$, $Ra = 1.68 \times 10^6 (= Ra^{\text{corr}})$, and $Nu = 5.97$, we plot a

numerical time sequence of a circulation $\Gamma(t)$ in Fig.12. Here,

$$\begin{aligned} \Gamma(t) = & R_L \oint_{\partial V} dx [v_x(x; L-d; t) - v_x(x; d; t)] - L \\ & + R_L \oint_{\partial V} dz [v_z(L-d; z; t) - v_z(d; z; t)] - L; \end{aligned} \quad (3.22)$$

where the integration is along a square contour with distance $d = 0.05L$ from the cell boundary. This quantity is positive for clockwise circulation and negative for counterclockwise circulation. In Fig.12, $\Gamma(t)$ is also plotted, which exhibits particularly large fluctuations on the occasion of orientation changes. This is a natural result because large-scale reorganization of the flow pattern is needed for an orientation change. Fig.13 illustrates the velocity patterns at $t = 228; 269$, and $311s$ in Fig.12. They closely resemble a picture of the measured velocity pattern in Ref. [22].

IV. SCALING THEORY

Rayleigh numbers realized in the existing simulations are still moderate in the sense that the plumes do not have enough kinetic energies such that they do not generate fully developed turbulence in the interior. In this pre-asymptotic regime of steady states, we may understand the numerical and experimental data using a very simple zeroth-order theory. First, we set $\phi_{p1} = \phi_{T1} = \phi_{v1}$ neglecting the possible small difference between ϕ_{T1} and ϕ_{v1} mentioned below (3.10). The plume sizes in the horizontal direction are also of order ℓ . Second, in our simulation the plumes are ejected into the interior with a velocity v_{p1} , for which the viscous drag and the buoyancy are balanced or

$$\rho v_{p1}^2 \approx g_p T: \quad (4.1)$$

Thus v_{p1} is of the order of the terminal velocity v_1 $Ra \propto v_1^3$ in (3.6) with $R = \ell$. In the interior we find that (i) gravity-induced acceleration of the plumes is suppressed by the viscous drag, (ii) $(v_x)^2 + (v_z)^2$ is nearly independent of z as stated below (3.10), and (iii) the last two terms on the left hand side of (2.17) are numerically of the same order. For example, the ratio of the average of $(\rho g T)^2$ in the x direction to that of $j(\rho v)^2$ is about 4 at $z = \ell$ and is fluctuating around 1 in the interior for the largest Q in Table 1. These support $v_{p1} \approx v_1$ in the interior. Third, to the sum rule (2.36) for the velocity gradients, the contribution from the boundary layers is of order $v_{p1}^2 = v_1^2$, while that from the interior is of order $\phi_{p1} v_{p1}^2 = v_1^2$ from (3.20). If use is made of (4.1) and the sum rule (2.36), these boundary-layer and bulk contributions become both of order $Ra Nu (D/L^2)^2$, which has also been confirmed numerically. Thus,

$$v_{p1} \approx Ra^{1/2} D/L; \quad (4.2)$$

$$Nu = L^{-1} = Pr^{-1} Ra^{1/4} : \quad (4.3)$$

These quantities are independent of Pr . In particular, the independence of Nu on Pr is consistent with the experiments [13,15,17]. Note that $v_{p1}(\lambda)$ is smaller than v_g in (3.4) by $Pr^{1/2}$.

Our height-dependent Reynolds number at $z = \lambda$ in (3.13) becomes

$$\hat{Re}(\lambda) = Ra^{1/4} = Pr : \quad (4.4)$$

The usual large-scale Reynolds number is given by $Re_{p1}L = Ra^{1/2} = Pr$. As $\hat{Re}(\lambda)$ exceeds a crossover value Re_{plum} , plumes will induce turbulence in the interior. Our simple scaling theory is valid for $Ra < (Re_{plum})^4$. In our simulation we have $\hat{Re}(\lambda) = 0.38Ra^{1/4}$, so that if we set $Re_{plum} = 10^3$ (regarding plumes as jets [34]), the upper bound is crudely estimated as 5×10^{13} . The transition from the scaling (4.3) to the asymptotic scaling occurs over a very wide range of Ra . Similarly, Grossmann and Lohse [6] considered a transition of a laminar boundary-layer flow to a turbulent boundary layer when the local Reynolds number on the scale of λ_v at $z = \lambda_v$ exceeds a value of order 420. Then Nu was claimed to be better expressed by

$$Nu = Ra^{1/4} (1 + C_1 Ra^b) \quad (4.5)$$

than the single power-law form, where C_1 and b are small coefficient and exponent, respectively, dependent on Ra and Pr under investigation (both being of order 0.1). This proposed form of Nu was later claimed to be in good agreement with data [14].

Here it would be informative to add more supplementary explanations of the previous scaling theories. (i) Shiraian and Siggia [2,3] assumed fully developed turbulence in the interior. Then the maximum of the turbulent velocity gradient is of order $S_d = k_d^2 = (v_{p1}^3 = L)^{1/2}$ at the smallest eddy size $k_d^{-1}(\lambda) = (\lambda)^{3/4} L^{1/4}$ if the Kolmogorov cascade is assumed with the energy dissipation rate $v_{p1}^3 = L$ [34] (the sparseness of ejected plumes being neglected). If the left hand side of the sum rule (2.36) is estimated as S_d^2 , it follows the relation,

$$v_{p1} = (Pr Nu Ra)^{1/3} D = L : \quad (4.6)$$

Furthermore, they assumed the linear horizontal velocity profile $v_x = (\lambda_0)z$ in the region $z < \lambda_T$, $L = Nu$, where λ_0 is given by (3.17). From the thermal diffusion equation $v_x @ T = @x = D r^2 T$ (the time-dependent fluctuations being neglected), they obtained the scaling,

$$\lambda_T^3 = \lambda_{p1}^2 = D L ; \quad (4.7)$$

by setting $@ = @x = L^{-1}$ and $r^2 = (@ = @z)^2 = \lambda_T^{-2}$ for a cell with $A = 1$. From (4.6) and (4.7) they found

$$Nu = Pr^{1/7} Ra^{2/7} : \quad (4.8)$$

However, as discussed below (3.14), our simulation suggests that the velocity deviates significantly from the linear profile in the boundary layers. (ii) Castaing et al. [5] assumed the balance (4.1) at the length λ_T ,

$$v_{p1} \lambda_T^2 g_p T = Ra Nu^2 D = L : \quad (4.9)$$

They furthermore assumed that the typical temperature scale in the interior is $(T)_c = \lambda_{p1}^2 = p g L$ and that the average heat current $(= Nu T = L)$ is of order $C_p (T)_c v_{p1}$. From these relations $(T)_c$ may be eliminated to give (4.6). If we combine (4.6) and (4.9), we are again led to (4.8). Therefore, to justify their arguments, the presence of fully developed turbulence in the interior seems to be required. (iii) Grossmann and Lohse [6,7] estimated the bulk and boundary-layer contributions to the sum rules for the temperature gradient and the velocity gradients, the incompressible version of (2.35) and (2.36). Their primary assumption is that the boundary layer thickness for the velocity is given by $\lambda_v = L = Re^{1/2}$ in terms of the large-scale Reynolds number Re [34]. Note that this assumption is not consistent with our zeroth-order scaling theory with respect to the Pr dependence. In particular, in the case where $Pr > 1$ and the boundary-layer contributions are dominant both for the temperature and the velocity, they obtained $Nu = Pr^{1/2} Ra^{1/4}$. In this case we also find $\lambda_v = \lambda_T = Pr^{1/3}$ from their theory. They predicted that this pre-turbulent scaling crosses over to the asymptotic turbulent scaling very slowly as in (4.5).

V. CONCLUDING REMARKS

We have presented a hydrodynamic model of compressible fluids properly taking into account the piston effect and the adiabatic temperature gradient effect. Though performed in two dimensions, our simulation has revealed some new effects unique in near-critical fluids, such as the overshoot behavior and the amplification of the overall temperature fluctuations as $T \rightarrow T_c$. It generally explains the experimental findings [16,17], but a discrepancy remains in the overshoot behavior at high heat flux Q as discussed in Section 3. It is desirable to extend simulation to smaller and higher Ra . Also more experiments on the overshoot and the temperature noises etc. are needed to resolve the discrepancy and to confirm the new predictions. As by-products, we have numerically examined steady state properties not treated in the previous simulations, such as the logarithmic velocity profile and the random reversal of macroscopic shear flow. They are universal aspects present both in compressible and incompressible fluids.

We have assumed that the fluid is in the supercritical region not very close to the critical point such that the conditions (2.1) and (2.2) are satisfied. However, if T

exceeds T_c or if T_{top} is below T_c , we encounter a variety of new effects such as boiling and wetting under heat flow and gravity [23,52]. We believe that such problems should provide us a new challenging field in which nonlinear dynamics and phase transition dynamics are coupled. These problems are beyond the scope of this paper.

We thank H. Meyer for valuable suggestions and comments. Thanks are also due to P. Tong for informative correspondence. This work is supported by Japan Space Forum grant H13-264.

-
- [1] S. Chandrasekhar, *Hydrodynamic and Hydromagnetic Stability* (Clarendon Press, Oxford, 1961).
- [2] E.D. Siggia, *Annu. Rev. Fluid Mech.* 26, 137 (1994).
- [3] B.I. Shraiman and E.D. Siggia, *Phys. Rev. A* 42, 3650 (1990).
- [4] L.P. Kadano, *Physics Today* 54, No.8, 34 (2001).
- [5] B. Castaing, G. Gunaratne, F. Heslot, L.P. Kadano, A. Libchaber, S. Thomae, Xiao-Zhong Wu, S. Zaleski, and G. Zanetti, *J. Fluid Mech.* 204, 1 (1989).
- [6] S. Grossmann and D. Lohse, *J. Fluid Mech.* 407, 27 (2000).
- [7] S. Grossmann and D. Lohse, *Phys. Rev. Lett.* 86, 3316 (2001).
- [8] The usual hydrodynamic equations for one-component fluids in the Boussinesq approximation are valid only when (i) the specific heat ratio $C_p = C_v$ is close to 1, (ii) T is much larger than $a_g L$ in (1.2), and (iii) the gravity-induced stratification is weak such that (2.2) holds.
- [9] M. Sano, Xiao-Zhong Wu, and A. Libchaber, *Phys. Rev. A* 40, 6421 (1989).
- [10] Xiao-Zhong Wu and A. Libchaber, *Phys. Rev. A* 45, 842 (1992).
- [11] S. Ashkenazi, Ph.D. thesis, Weizmann Institute of Science, Rehovot, Israel, 1997 (unpublished); S. Ashkenazi and V. Steinberg, *Phys. Rev. Lett.* 85, 3641 (1999).
- [12] X. Chavanne, Ph.D. thesis, Université Joseph Fourier, Grenoble, 1997 (unpublished).
- [13] X. Chavanne, F. Chilla, B. Castaing, B. Hebral, B. Chabaud and J. Chaussy, *Phys. Rev. Lett.* 79, 3648 (1997); X. Chavanne, F. Chilla, B. Chabaud, B. Castaing, and B. Hebral, *Phys. Fluids* 13, 1300 (2001).
- [14] X. Xu, K.M.S. Bajaj and G. Ahlers, *Phys. Rev. Lett.* 84, 4357 (2000).
- [15] G. Ahlers and X. Xu, *Phys. Rev. Lett.* 86, 3320 (2001).
- [16] A.B. Kogan, D. Murphy and H. Meyer, *Phys. Rev. Lett.* 82, 4635 (1999).
- [17] A.B. Kogan and H. Meyer, *Phys. Rev. E* 63, 056310 (2001).
- [18] J.J. Niemela, L. Skrbek, K.R. Sreenivasan and R.J. Donnelly, *Nature* 404, 837 (2000).
- [19] J.J. Niemela, L. Skrbek, K.R. Sreenivasan and R.J. Donnelly, *J. Fluid Mech.* 449 169 (2001).
- [20] B.J. Glickman, H. Wilhelm, and J.P. Gollub, *Phys. Fluids A* 5, 647 (1993).
- [21] S. Cioni, S. Ciliberto, and J. Sommeria, *J. Fluid Mech.* 335, 111 (1997).
- [22] X.-L. Qiu and P. Tong, *Phys. Rev. E* 64, 036304 (2001).
- [23] A. Onuki, *Phase Transition Dynamics*, (Cambridge University Press, Cambridge, 2002).
- [24] A. Onuki and R.A. Ferrell, *Physica A* 164, 245 (1990); A. Onuki, H. Hao and R.A. Ferrell, *Phys. Rev. A* 41 2256 (1990).
- [25] J. Straub and K. Nitsche, *Fluid Phase Equilibria*, 88, 183 (1993). J. Straub, L. Eicher and A. Haupt, *Phys. Rev. E* 51, 5556 (1995).
- [26] H. Boukari, J.N. Shaumeyer, M.E. Briggs and R.W. Gammon, *Phys. Rev. A* 41, 2260 (1990).
- [27] B. Zappoli, D. Bailly, Y. Garrabos, B. Le Neindre, and D. Beysens, *Phys. Rev. A* 41, 2264 (1990).
- [28] P. Guenoun, B. Khalil, D. Beysens, F. Kamoun, B. Le Neindre, Y. Garrabos and B. Zappoli, *Phys. Rev. E* 47 1531, (1993)
- [29] F. Zhong and H. Meyer, *Phys. Rev. E* 51, 3223 (1995)
- [30] S. Amiroudine, P. Bontoux, P. Larmoud, B. Gilly and B. Zappoli, *J. Fluid Mech.* 442, 119 (2001).
- [31] Y. Chivata and A. Onuki, *Phys. Rev. Lett.* 87, 144301 (2001).
- [32] M. Gitterman and V. Steinberg, *J. Appl. Math. Mech. USSR* 34, 305 (1971); M. Gitterman, *Rev. Mod. Phys.* 50, 85 (1978).
- [33] P. Carles and B. Ugurtas, *Physica D*, 126, 69 (1999).
- [34] L.D. Landau and E.M. Lifshitz, *Fluid Mechanics* (Pergamon, 1959).
- [35] E.E. DeLuca, J. Weme, and R. Rosner, *Phys. Rev. Lett.* 64, 2370 (1990); J. Weme, E.E. DeLuca, R. Rosner, and F. Cattaneo, *ibid.* 67, 3519 (1991).
- [36] U. Hansen, D.A. Yuen and S.E. Kroening, *Phys. Fluids A* 2, 2157 (1990); U. Hansen, D.A. Yuen and A.V. Malevsky, *Phys. Rev. A* 46, 4742 (1992). Here the Stokes approximation was used in the range $10^6 < Ra < 10^9$ in 2D. Nevertheless they could obtain the scaling (1.5) in agreement with the experiments, which suggests that the balance of the viscous drag and the buoyancy in (4.1) should have also been realized in the experiments.
- [37] S. Balachandar and L. Sirovich, *Phys. Fluids A* 3, 919 (1991).
- [38] S. Toh and E. Suzuki, *Unstable and Turbulent Motion of Fluid*, (World Scientific, 1993) p. 272.
- [39] C. Bizon, J. Weme, A.A. Predtechensky, K. Julien, W.D. McCormick, J.B. Swift and H.L. Swinney, *Chaos* 7, 107 (1997).
- [40] S.L. Christie and J.A. Domaradzki, *Phys. Fluids A* 5, 412 (1993).
- [41] R. Verzicco and R. Camussi, *J. Fluid Mech.* 383, 55 (1999).
- [42] R.M. Kerr, *J. Fluid Mech.* 310, 139 (1996).
- [43] R.M. Kerr and J.R. Herring, *J. Fluid Mech.* 419, 325 (2000).
- [44] For $0 < \epsilon < 1$ the scaling form $p = G(u)$ holds with $u = (\epsilon - 1) = \dots$. For $\epsilon > 1$ or under (2.2) in gravity, we have $G(u) = G(0)$ and $p = G(0)$.
- [45] G.P. Metcalfe and R.P. Behringer, *J. Low Temp. Phys.* 78, 231 (1990).
- [46] To be precise, the time constant of the pressurehomogenization is given by $t_{hom} = (t_{act})^{1/2}$ under the

condition $t_{ac} = t_l$ in terms of the acoustic time $t_{ac} = L/c$ and the piston time t_l [23]. Here the damping of the pressure oscillation is mainly caused by the damping of the oscillatory heat current in the thermal diffusion layers.

[47] L.D. Landau and E.M. Lifshitz, *Statistical Physics* (Pergamon, New York, 1964), Chap.12. It is well-known that the thermal fluctuations of T and ϕ obey the Gaussian distribution proportional to $\exp(-F/k_B T)$, where F is given by (2.20). See Ref. [23] for more discussions on this aspect.

[48] G. Ahlers, M.C. Cross, P.C. Hohenberg, and S. Saffman, *J. Fluid Mech.* **110**, 297 (1981).

[49] A. Schuster, D. Lortz and F. Busse, *J. Fluid Mech.* **23**, 129 (1965).

[50] R.P. Behringer and G. Ahlers, *Phys. Lett. A* **62**, 329 (1977). This experiment was performed in ^4He at $T = 2.184\text{K}$ at saturated vapor pressure. Here the fluid is nearly incompressible and $\beta_s = 1$.

[51] H. Meyer and A.B. Kogan, preprint.

[52] A. Onuki, preprint.

TABLE I. Parameters at $\beta_s = 0.05$ in steady states for periodic sidewalls

Q (W/cm s)	T (mK)	Ra^{corr}	Ra	Nu_1	\overline{Re}
0.0458	0.0154	$3.43 \cdot 10^3$	$6.69 \cdot 10^3$	0.714	0.655
0.965	0.135	$5.87 \cdot 10^4$	$5.54 \cdot 10^4$	3.04	3.035
122.2	6.89	$2.91 \cdot 10^6$	$2.91 \cdot 10^6$	9.29	7.89

Fig.1. $T(t)$ vs time (solid line) calculated from (2.8) and (2.17) for (a) $Q = 0.965$ $W = \text{cm}^2$ and (b) $Q = 122.2$ $W = \text{cm}^2$. The temperature profiles for the points (2) on the curve in (b) are given in Fig.2. The experimental data (+) [17] are shown in (b). The upper broken curves in (a) and (b) represent the theoretical result (3.3) obtained from integration of (2.8) with $v = 0$. The dotted curves represent the numerical ones in the fixed pressure condition without the piston effect.

Fig.2. Temperature profiles at (A), (B), (C), (D), (E), and (F) on the curve of $Q = 122.2$ $W = \text{cm}^2$ in Fig.1b (2). The temperature (and velocity) deviations are more enhanced in the transient states (A)–(E) than in a steady state (F). The T at the bottom boundary $z = 0$ is equal to $T(t)$ in Fig.1b. The plumes tend to be connected between bottom and top because $Pr = 7.4$.

Fig.3. Time evolution of $\overline{T}(z;t)$ defined by (3.5) at the points (A), (C), (E), and (F) in Fig.1b for $Q = 122.2$ $W = \text{cm}^2$.

Fig.4. Numerical results of $Ra(Nu - 1) = (Ra^{\text{corr}} - Ra_c)$ vs $Ra^{\text{corr}} = Ra_c - 1$ in steady states, obtained under the periodic boundary condition (+) and for $A = 3(2); 2()$; and $1()$. The first curve (+) is close to the experimental results for $A = 57$ [17] (solid line) and is well fitted to the scaling form (1.5) with $a = 2=7$ for $Ra^{\text{corr}} = Ra_c > 10$. With decreasing the aspect ratio A , crossover to the scaling occurs at much larger Ra^{corr} .

Fig.5. Height-dependent average temperature profiles $\overline{T}(z)$ divided by T in steady states for the three Q values in Table 1. The arrows represent the maxima of $v_x(z)$ in Fig.6a.

Fig.6. Normalized height-dependent variances, $v_x(z) = v_g$ for the horizontal velocity in (a) and $v_z(z) = v_g$ for the vertical velocity in (b) in steady states for the three Q values in Table 1.

Fig.7. Overall Reynolds number \overline{Re} defined by (3.11) as a function of $Ra^{\text{corr}} = Ra_c - 1$ in steady states for $Q = 122.2$ $W = \text{cm}^2$.

Fig.8. Height-dependent Reynolds number $\hat{Re}(z)$ defined by (3.9) in steady states for the three Q values in Table 1.

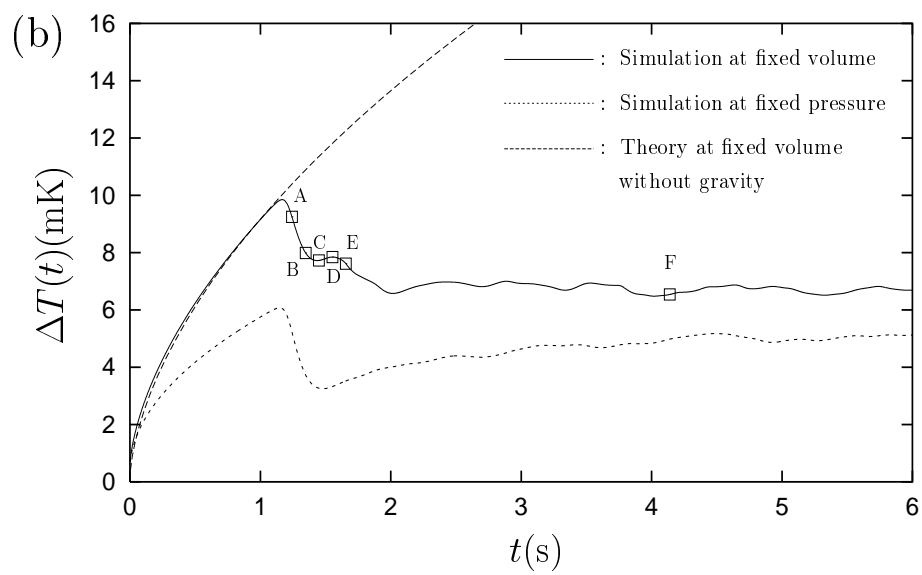
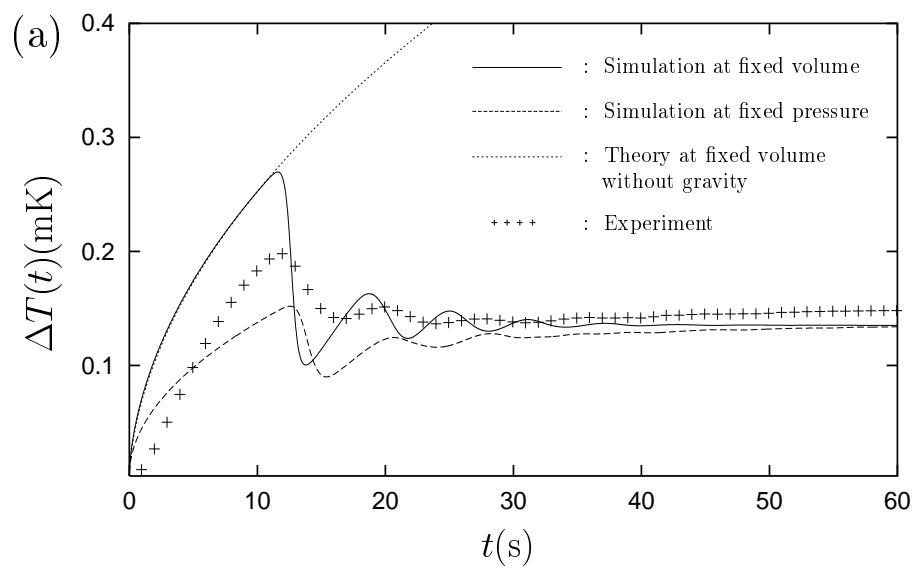
Fig.9. (a) Height-dependent velocity variance $v_x(z)$ defined by (3.9) on a semi-logarithmic scale in steady states for $Q = 122.2$ $W = \text{cm}^2$. (b) $v_x(z)$ (upperline) and velocity gradient variance $zD_{xz}(z)$ defined by (3.15) (lower line) on a logarithmic scale.

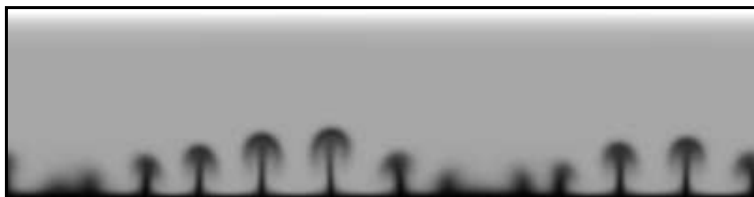
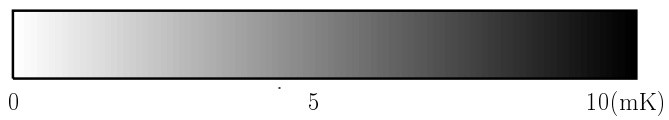
Fig.10. Snapshots of the normalized velocity variance $v_z(x;t) = v_g$ averaged in the z direction defined by (3.17) for the three values of Q in Table 1. The system is periodic with period $4L$ in the x direction. The peak heights increase with increasing Q . For the largest Q this quantity changes in time as the plumes move in the cell, while for the other Q it is weakly dependent on or independent of time.

Fig.11. $hTi(t)$ and $T(t)$ at fixed volume (solid line) and at fixed pressure (broken line) for $\beta = 0.05$ (upper figure) and 0.01 (lower figure). The noises of these quantities at fixed volume increase as the reduced temperature is decreased.

Fig.12. Time evolution of the circulation $\Gamma(t)$ defined by (3.22) (upper figure) and $T(t)$ (lower figure) for $Q = 122.2$ $W = \text{cm}^2$ in a cell with $A = 1$. The orientation of the macroscopic flow changes on a time scale of 50 s. The sign of $\Gamma(t)$ represents the orientation of the macroscopic circulation, while the fluctuations of $T(t)$ become large when the orientation changes.

Fig.13. Velocity patterns at $t = 228; 269$, and 311 s for the run in Fig.12. At $t = 228$ s the orientation is counter-clockwise, while at $t = 311$ s it is clockwise. At $t = 269$ s two large eddies with different orientations can be seen.





A $t = 1.24$ s



B $t = 1.38$ s



C $t = 1.45$ s



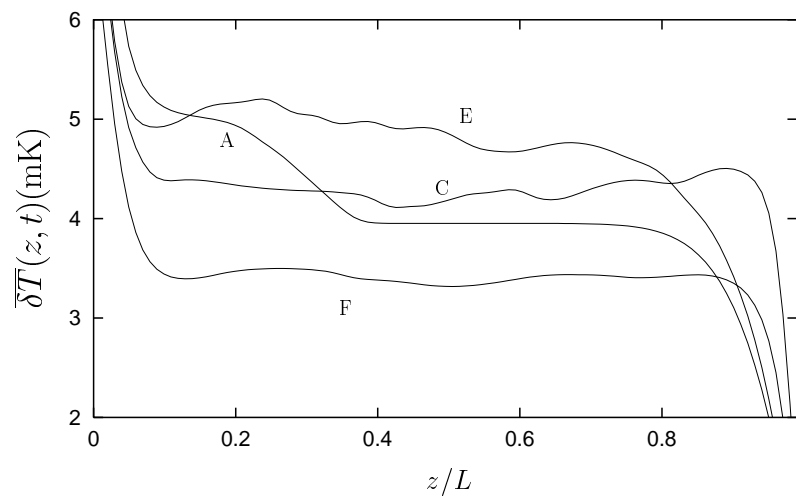
D $t = 1.55$ s

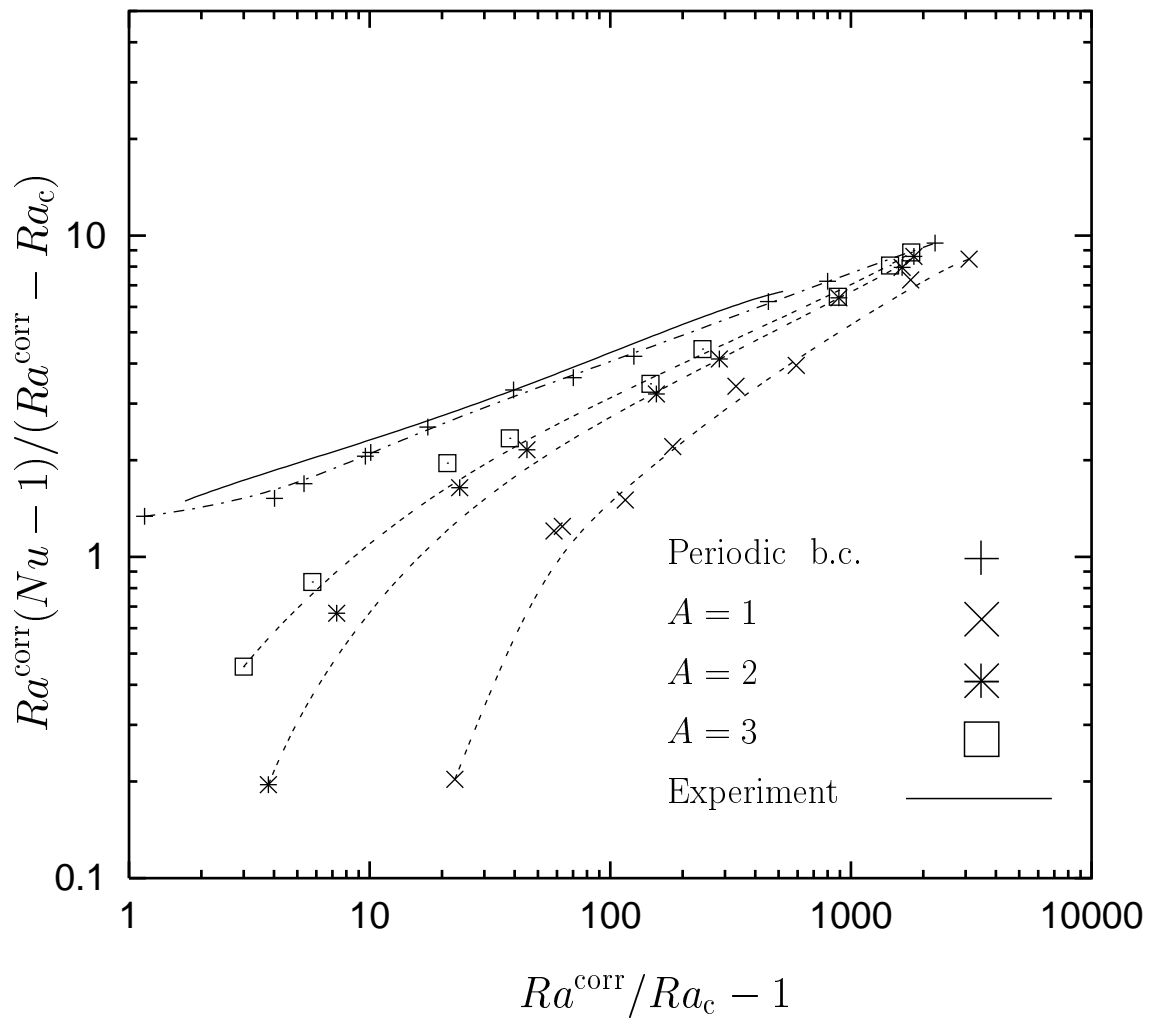


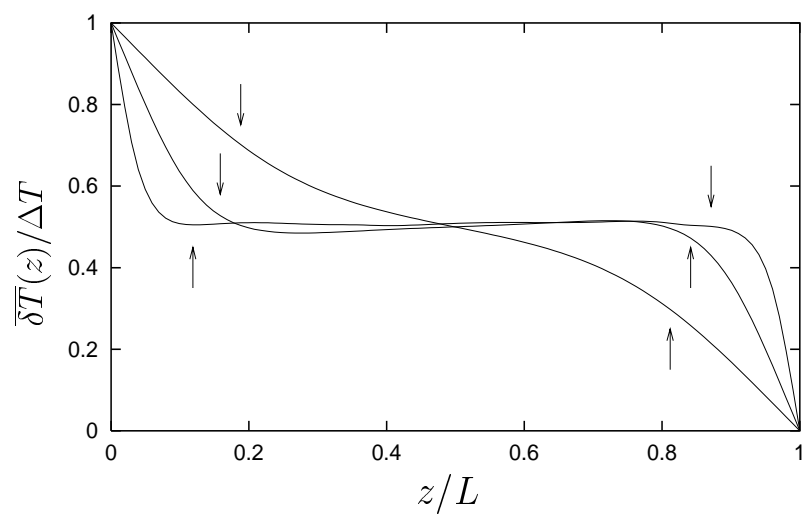
E $t = 1.66$ s

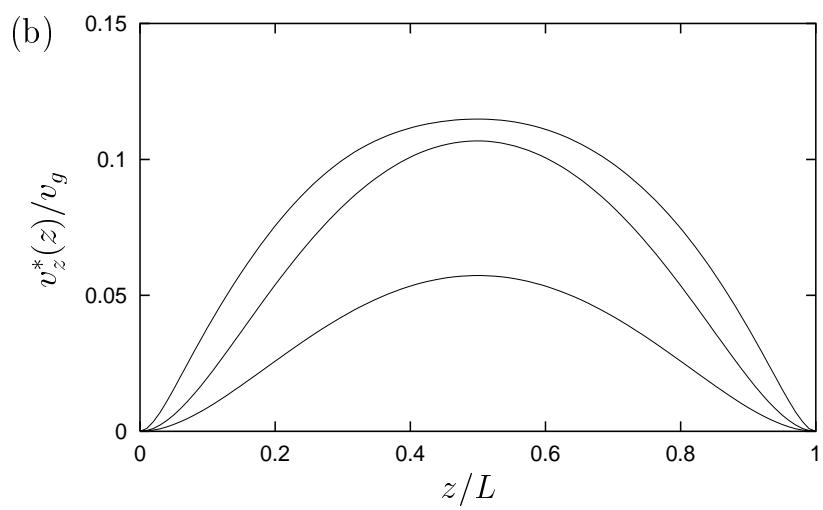
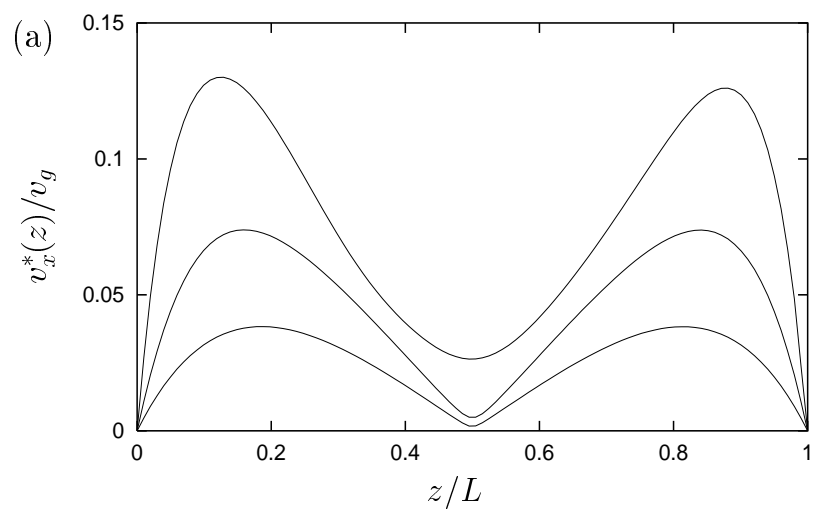


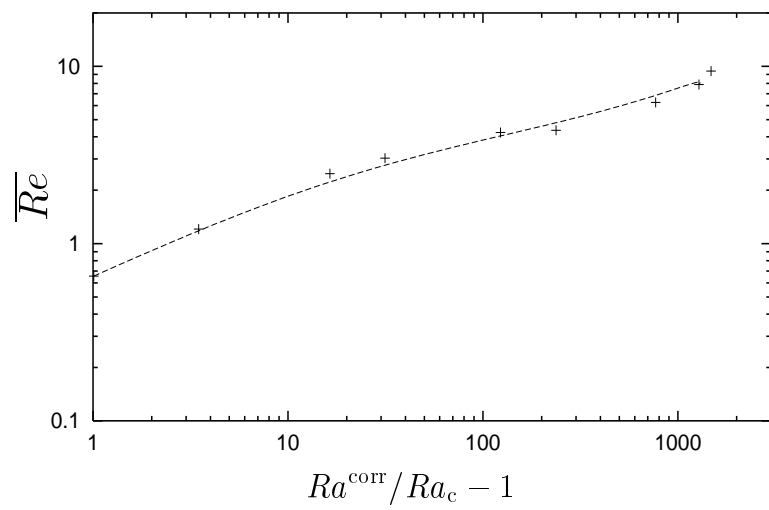
F $t = 4.14$ s

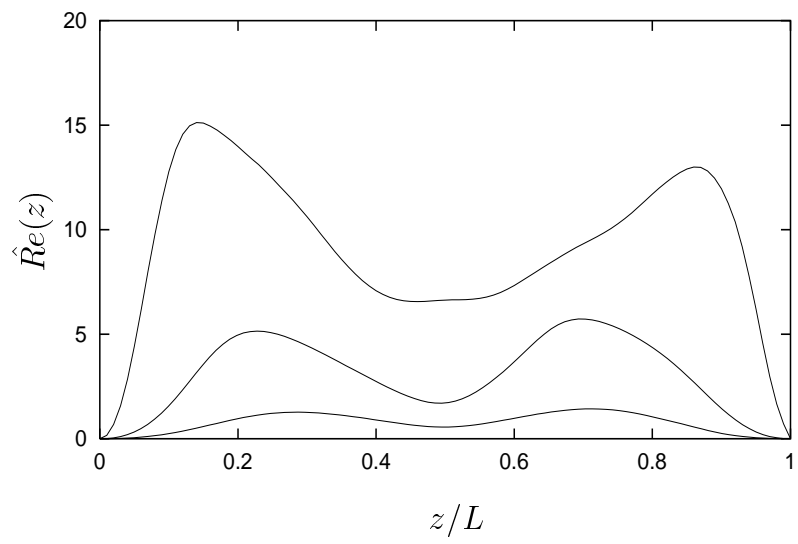




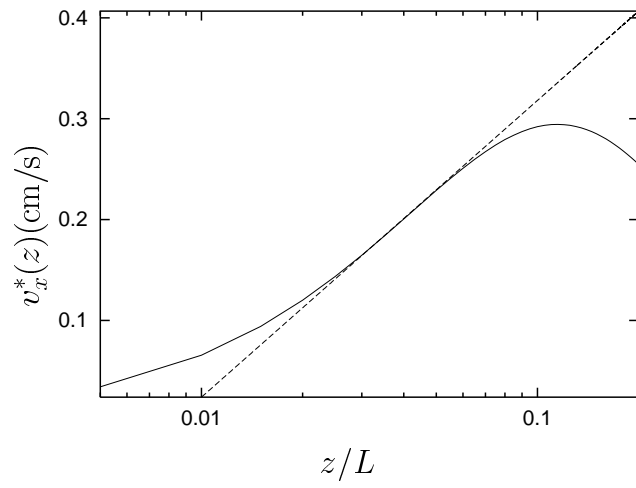




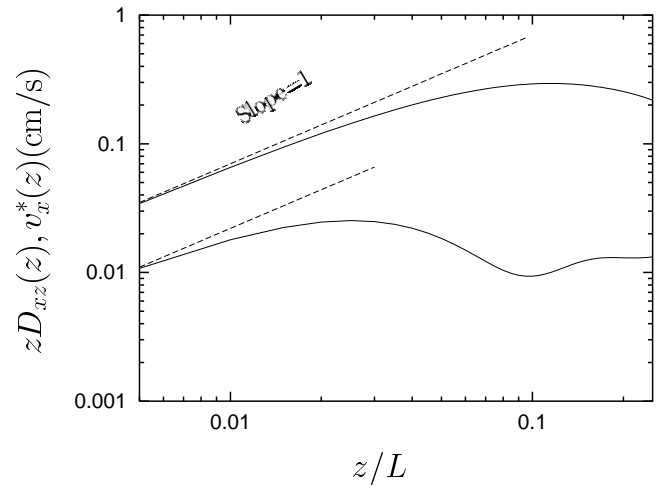


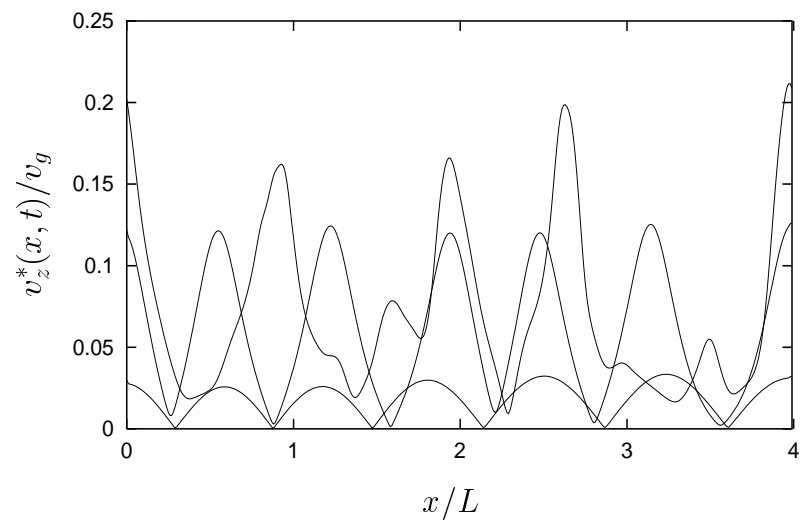


(a)

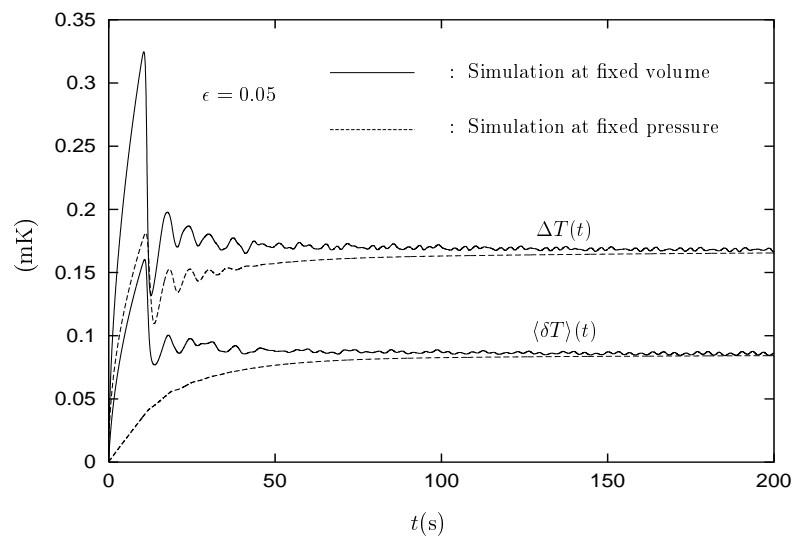


(b)

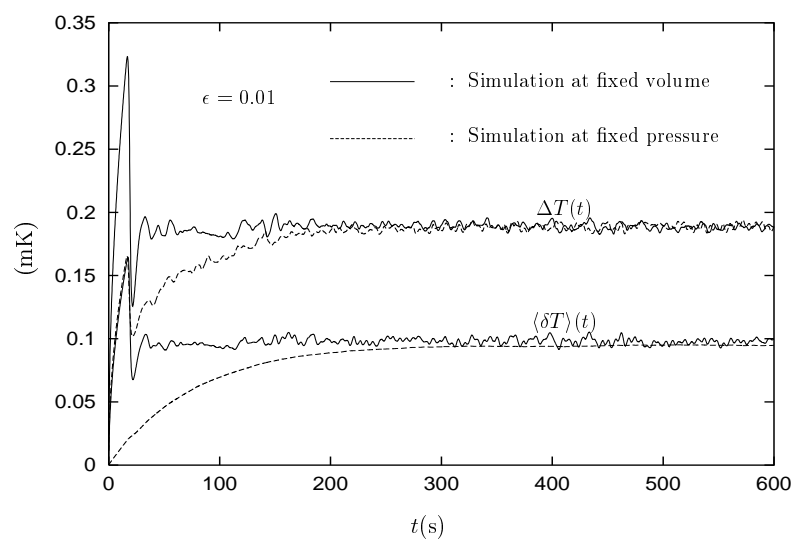


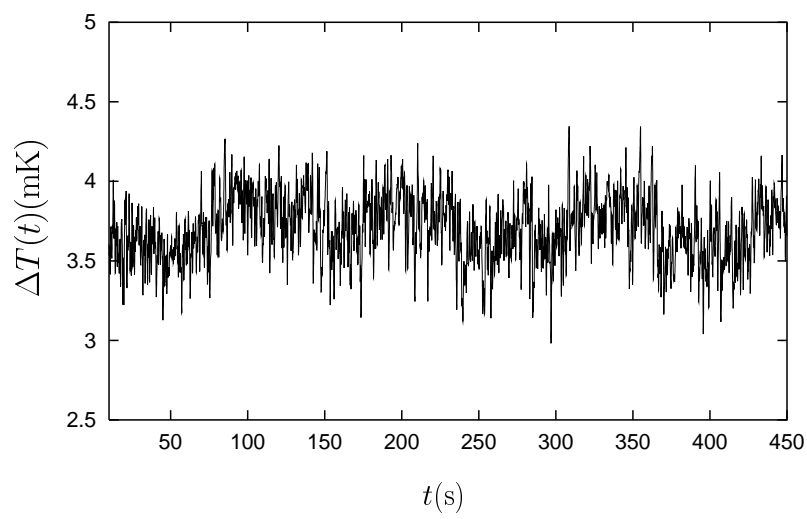
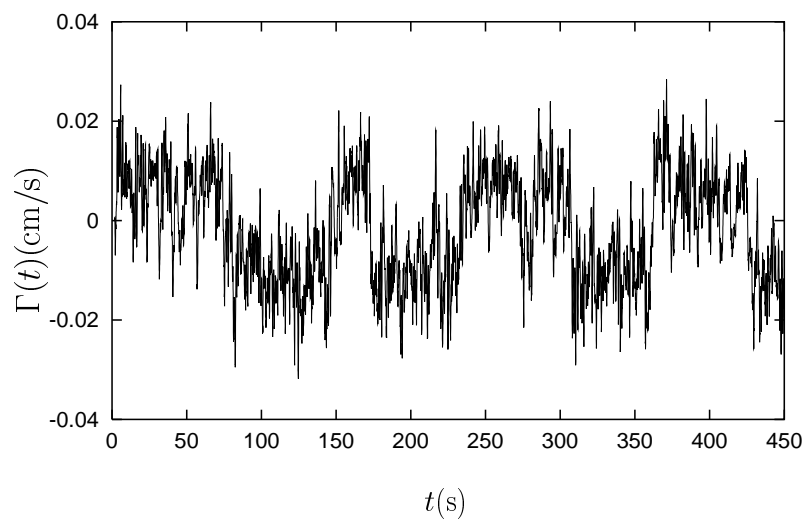


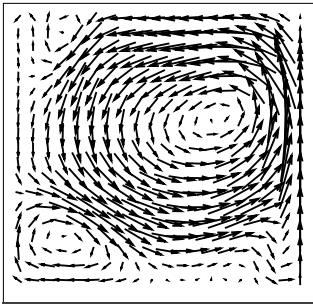
(a)



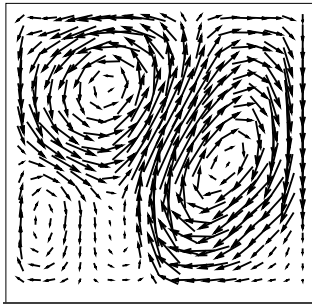
(b)



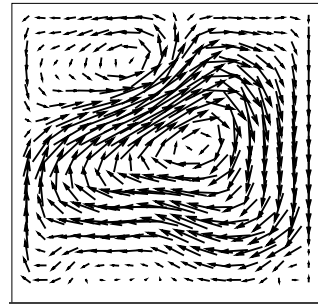




$t = 228 \text{ s}$



$t = 269 \text{ s}$



$t = 311 \text{ s}$